scientific reports

Check for updates

OPEN

Design and application of a magnetically recoverable citric acid-functionalized graphene oxide nanocomposite for ultrasound-assisted green synthesis of naphthopyrimidines

Raziyeh Molla-Mohammadi, Javad Safaei-Ghomi✉ & Hourieh Sadat Oboudatian

This study reports the synthesis of a novel acidic and magnetic nanocatalyst based on graphene oxide (GO), iron oxide (Fe_3O_4), and silica (SiO_2), functionalized with citric acid (CA), which was successfully synthesized and characterized by FT-IR, XRD, SEM, TEM, EDX, TGA, VSM, and Raman spectroscopy. The resulting nanocomposite (GO/Fe_3O_4@SiO_2@CA) exhibited a well-defined core–shell structure, high thermal stability, and superparamagnetic properties. This material was employed as a recyclable and green catalyst for the one-pot multicomponent synthesis of naphthopyranopyrimidines derivatives in ethanol under ultrasonic conditions. The catalyst showed excellent efficiency, product yields (88–97%) within remarkably short times (10–20 min), and was easily recoverable by an external magnet. Additionally, it was able to retain its catalytic activity over seven consecutive cycles with negligible loss in performance. These results highlight GO/Fe_3O_4@SiO_2@CA as a sustainable and high-performance nanocatalyst for green organic synthesis. In this study, we synthesized a mild, non-toxic, green, and multi-acid catalyst, and were able to increase the product formation efficiency and reduce the time with cavitation energy. It seems that this catalyst has the potential to be used for the preparation of other one-pot products.

Keywords Naphthopyranopyrimidines, Magnetic nanoparticles, Multicomponent reactions, Green synthesis, Hummers' method, Nanocomposite, Graphene oxide

Nanocomposites have gained considerable attention in recent years due to their remarkable physicochemical properties, such as high surface area, tunable chemical functionality, and excellent stability. These features make them suitable for a wide range of applications, including catalysis, energy conversion, drug delivery, and environmental remediation[1–3]. Among nanostructured supports, graphene oxide (GO), a two-dimensional oxidized form of graphite, is particularly appealing because of its large surface area, strong mechanical properties, and abundant oxygenated functional groups (–OH, –COOH, and epoxy), which allow strong interactions with both organic and inorganic molecules[4–9]. The rich surface chemistry of GO provides multiple anchoring sites for metal and metal oxide nanoparticles through coordination and hydrogen bonding. Oxygen groups on GO act as nucleation centers for Fe_3O_4 nanoparticles, promoting uniform dispersion and preventing magnetic aggregation. Coating Fe_3O_4 with silica (SiO_2) forms a protective shell that enhances thermal and chemical stability while maintaining access to active sites[10–14]. Functionalization of the composite with citric acid (CA), a biocompatible organic acid, introduces additional –COOH and –OH groups, increasing polarity, hydrophilicity, and surface reactivity. The selection of citric acid was made based on the higher density of acidic sites, controlled acidity compared to strong acids Includes of sulfonic group and green chemistry considerations. Citric acid contains three carboxylic acid groups, through which multiple Brønsted acidic sites can be introduced onto the catalyst surface. As a result, enhanced surface acidity and possible cooperative catalytic interactions are provided compared to mono-functionalized systems. As citric acid is recognized as an inexpensive, biodegradable, non-

Department of Organic Chemistry, Faculty of Chemistry, University of Kashan, P.O. Box 87317-51167, Kashan, I. R. of Iran. ✉email: safaei@kashanu.ac.ir

toxic, and industrially abundant organic acid. Therefore, improved sustainability and better alignment with green chemistry principles are achieved through its incorporation.

The resulting nanocomposite, GO/Fe_3O_4@SiO_2@CA, combines the electronic conductivity and mechanical strength of GO, the magnetic responsiveness of Fe_3O_4, and the chemical stability of SiO_2, producing a multifunctional catalyst with high activity and recyclability[15–20]. GO also plays a central role as an electron mediator. Its two-dimensional π-conjugated structure enables rapid electron delocalization, enhancing charge transfer between active sites and reactants. Strong π–π stacking and hydrogen bonding interactions further allow efficient adsorption of aromatic molecules such as β-naphthol and aldehydes, improving catalytic efficiency even under mild ultrasonic irradiation[21–27].

Multicomponent reactions (MCRs) have emerged as highly sustainable strategies for constructing complex heterocycles with high atom economy and minimal waste. Pyranopyrimidines and their fused derivatives, including naphthopyranopyrimidines, are bioactive heterocycles with diverse pharmacological properties, including anticancer, antimicrobial, and anti-inflammatory effects. Traditional synthetic methods often require long reaction times, toxic solvents, and non-recyclable catalysts[28–36]. In this study, we report the synthesis and characterization of a novel citric acid-functionalized magnetic nanocomposite, GO/Fe_3O_4@SiO_2@CA, prepared via a modified Hummers' method. Its catalytic potential was evaluated in the green, one-pot multicomponent synthesis of naphthopyranopyrimidine derivatives under ultrasonic irradiation in ethanol. Efficient magnetic separation and good recyclability are exhibited by the prepared nanocomposite. Catalytic performance is maintained over multiple reaction cycles, further distinguishing the developed system from previously reported catalysts. The cooperative effects of GO, Fe_3O_4, SiO_2, and CA resulted in high catalytic activity, excellent yields, easy magnetic recovery, and remarkable structural stability, offering a sustainable and efficient approach for the synthesis of bioactive heterocycles. We also investigated the synergistic effect with ultrasonic. The combination of polycarboxylic acid functionality, magnetic graphene oxide support, and ultrasonic irradiation provides a synergistic catalytic system. Ultrasound-induced cavitation enhances mass transfer and accessibility of acidic sites, resulting in shorter reaction times and improved yields compared to conventional conditions. The use of ultrasonic irradiation significantly reduced reaction time while maintaining high yield and selectivity. Also, we managed to synthesize some new derivatives (six compounds) of naphthopyranopyrimidines.

Experimental section

Chemicals and methods

All materials, including solvents and reagents, met analytical-grade specifications and were applied directly in the procedures without any pre-treatment. Natural graphite powder, ferric chloride hexahydrate ($FeCl_3{\cdot}6\ H_2O$), ferrous sulfate heptahydrate ($FeSO_4{\cdot}7\ H_2O$), tetraethyl orthosilicate (TEOS), citric acid (CA), and ammonia solution were purchased from Merck and Sigma-Aldrich. Deionized water was employed throughout all experiments. Graphene oxide and all nanocomposites were characterized using FT-IR (Shimadzu 8400 s), ^1H and ^{13}C NMR (DMSO), XRD (Philips PW1730), SEM and TEM (ZEISS), VSM (Meghnatis Daghigh Kavir), and TGA (STA504).

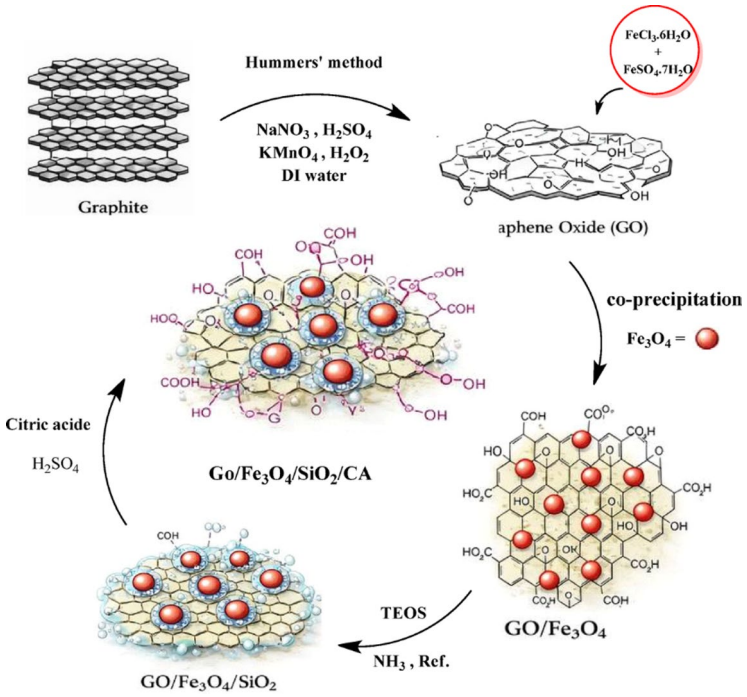
Preparation of graphene oxide (GO)

Graphene oxide (GO) was synthesized from natural graphite powder using a modified Hummers' method, chosen for its simplicity, reproducibility, and ability to produce high-quality GO with abundant oxygen-containing functional groups. In a typical procedure, 2 g of natural graphite and 1 g of sodium nitrate ($NaNO_3$) were added to 46 mL of concentrated sulfuric acid (H_2SO_4, 98%) in an ice bath. Sulfuric acid provides a strong acidic medium that facilitates intercalation between graphite layers and controls the oxidation process. Sodium nitrate promotes layer separation, ensures uniform oxidation, prevents aggregation, and improves the overall quality of GO. Next, 6 g of potassium permanganate ($KMnO_4$) was added gradually under continuous stirring while keeping the temperature below 35 °C to avoid excessive heat generation. $KMnO_4$ acts as a strong oxidizing agent that converts graphite into graphene oxide and introduces oxygen-containing functional groups (–OH, –COOH, epoxy) onto the surface. The reaction mixture was stirred at this temperature for 2 h to ensure complete oxidation. Afterwards, 92 mL of deionized water was slowly added, and the reaction continued for 30 min. To further dilute the mixture and terminate the oxidation, 280 mL of deionized water was added, followed by 20 mL of hydrogen peroxide (H_2O_2, 30 wt%).

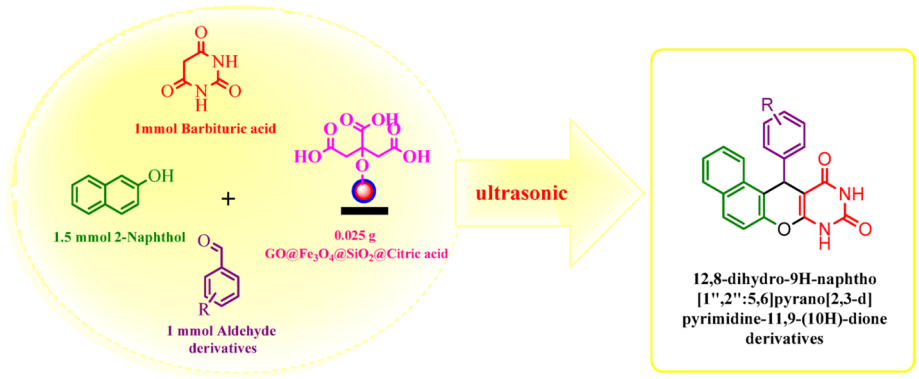
The addition of H_2O_2 turned the suspension golden, indicating the removal of residual $KMnO_4$ and MnO_2. Hydrogen peroxide stops the oxidation reaction, removes remaining oxidants, stabilizes the GO suspension, and enhances surface oxygen functionalities. The resulting black solid was repeatedly washed with warm deionized water and ethanol to remove residual acids and impurities. The suspension was ultrasonicated for 45 min to ensure uniform dispersion of the GO sheets. Finally, the mixture was centrifuged, and the obtained product was dried in oven at 50 °C for 12 h, yielding high-quality graphene oxide powder. The entire procedure ensures the formation of GO with high surface area, abundant functional groups, and good dispersibility, suitable for subsequent nanocomposite synthesis in Scheme 1[37–42].

Preparation of GO/Fe_3O_4 nanocomposite

Fe_3O_4 nanoparticles were deposited onto GO sheets via a co-precipitation method. Briefly, GO (0.5 g) was dispersed in 100 mL of deionized water and sonicated for 30 min to form a homogenous suspension. $FeCl_3{\cdot}6\ H_2O$ (2.7 g) and $FeSO_4{\cdot}7\ H_2O$ (1.0 g) were added to the GO suspension under inert nitrogen conditions. Ammonia solution was added dropwise to adjust pH ~ 10. The mixture was stirred at 80 °C for 2 h, resulting in the formation of Fe_3O_4 nanoparticles on the GO sheets. The black product was magnetically separated, thoroughly washed with water and ethanol, and dried at 60 °C in Scheme 1[37,43].



Scheme 1. The preparation of GO/Fe_3O_4@SiO_2@CA nanocomposite.



Scheme 2. Synthesis of 12,8-Dihydro-9H-naphtho[1",2":5,6]pyrano[2,3-d]pyrimidine-11,9-(H10)-dione Derivatives Using GO/Fe_3O_4@SiO_2@Citric Acid Nanocatalyst Under Ultrasonic Irradiation Conditions.

Coating of GO/Fe_3O_4 with silica (SiO_2)

The synthesized GO/Fe_3O_4 composite was dispersed in ethanol–water mixture under ultrasonication to achieve a uniform suspension. Tetraethyl orthosilicate (TEOS, 1 mL) and NH_4OH were then added dropwise, and the reaction was allowed to proceed under continuous stirring at room temperature for 24 h. The GO/Fe_3O_4@SiO_2 nanocomposite was recovered by magnetic separation, followed by repeated washing and drying in Scheme 1[44–47].

Functionalization with citric acid (CA)

For surface functionalization, 0.5 g of GO/Fe_3O_4@SiO_2 was treated with 1 g of citric acid dissolved in 50 mL of water and stirred at 60 °C for 4 h. After the reaction, the GO/Fe_3O_4@SiO_2@CA nanocatalyst was isolated using an external magnet, repeatedly washed with ethanol and water, and dried under vacuum at 60 °C in Scheme 1.

General procedure for synthesis of naphthopyranopyrimidines

In a 10 mL ethanol solution, β-naphthol (1 mmol), benzaldehyde derivatives (1 mmol), barbituric acid (1 mmol), and 20 mg of GO/Fe_3O_4@SiO_2@CA were mixed and stirred at 60 °C. In some experiments, ultrasonic irradiation was used. Reaction progress was monitored via TLC. Upon completion, the catalyst was magnetically separated, washed, and reused for subsequent runs. The crude product was filtered, washed with cold ethanol, and recrystallized to obtain pure naphthopyranopyrimidine derivatives in Scheme 2.

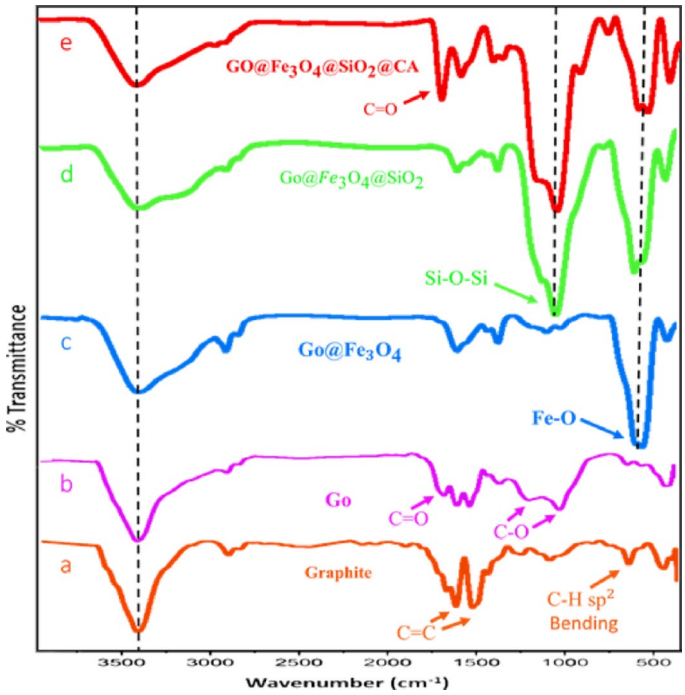


Fig. 1. FT-IR spectra of (a) Graphite, (b) GO, (c) GO@Fe_3O_4, (d) GO@Fe_3O_4@SiO_2,(e) GO@Fe_3O_4@SiO_2@CA.

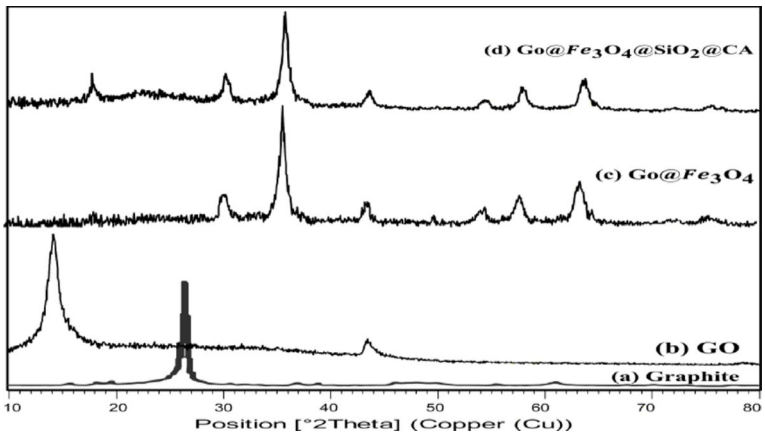


Fig. 2. XRD patterns of graphite, GO, GO@Fe_3O_4, and GO@Fe_3O_4@SiO_2@CA.

Results and discussion

Structural and morphological characterization of GO/Fe_3O_4@SiO_2@CA nanocomposite

The structural characteristics and chemical functionalities of the synthesized nanocomposite were investigated using various analytical techniques. The FT-IR spectra of graphite and of GO-based nanocomposites (GO, GO/Fe_3O_4, GO/Fe_3O_4@SiO_2, GO/Fe_3O_4@SiO_2@CA) were acquired and shown in Fig. 1. In Fig. 1b, the broad absorption band at 3430 cm^{-1} corresponds to O–H stretching vibrations. Distinct peaks at 1720 and 1625 cm^{-1} are attributed to C = O and C = C bonds, respectively. A new peak observed at 580 cm^{-1} indicates the Fe–O vibration (Fig. 1c), while characteristic Si–O–Si bands appear around 1100 cm^{-1} (Fig. 1d). In the final catalyst, peaks near 2925 cm^{-1} (sp^3–CH) and 1750 cm^{-1} (carboxylic acid C = O) confirm the effective functionalization with citric acid (Fig. 1e). The data obtained from FT-IR spectra indicated the correct deposition and formation of GO@Fe_3O_4@SiO_2@CA nanocomposite.

The powder X-ray diffraction (XRD) of (a) graphite, (b) GO, (c) GO@Fe_3O_4, and (d) GO@Fe_3O_4@SiO_2@CA displays in Fig. 2. XRD patterns showed a sharp peak at $2\theta \approx 27°$ for pristine graphite (Fig. 2a) and a broad peak at $\approx 14°$ after oxidation, confirming GO formation (Fig. 2b). Peaks at $2\theta = 30.1°$, 35.6°, 43.3°, 53.5°, 57.2°, and 62.8° correspond to Fe_3O_4 spinel structure (JCPDS No. 75–0449)(Fig. 2c). In the final pattern, a broad background

around 20°–25° indicates amorphous groups of SiO_2 and citric acid (Fig. 2d). These results and the constant of Fe_3O_4 pattern in Fig. 2d, confirm the successful stepwise assembly of the nanocomposite (Fig. 2).

In order to study the morphology, uniformity and size of the catalyst, the FE-SEM and TEM were used. As it is obvious in Fig. 3b, the FE-SEM images demonstrated that spherical Fe_3O_4 nanoparticles, with an average size of about 63 nm, were uniformly distributed across the surface of GO sheets. TEM analysis further confirmed the presence of Fe_3O_4@SiO_2@CA at their interface with GO (Fig. 3c).

All elements are well distributed throughout the graphene oxide and GO@Fe_3O_4@SiO_2@CA nanocomposite, which are revealed by elemental mapping images (Fig. 4a, b). Besides, the presenting elements along with weight% can be clearly seen in the structure of graphene oxide and GO@Fe_3O_4@SiO_2@CA nanocomposite using energy dispersive X-ray spectroscopy (EDX) (Fig. 4c, d). Elemental mapping by EDX revealed a homogeneous distribution of carbon, oxygen, iron, and silicon elements throughout the catalyst structure.

The magnetic properties of GO@Fe_3O_4 and GO@Fe_3O_4@SiO_2@CA have been measured with the help of a vibrating sample magnetometer (VSM) (Fig. 5). Magnetization measurements revealed that GO/Fe_3O_4 had a saturation magnetization of ~ 60 emu/g, while GO/Fe_3O_4@SiO_2@CA showed ~ 40 emu/g due to surface modifications and silica shell. These results illustrate that the magnetization property decreases by coating and functionalization. Besides, the nanocomposite retained sufficient superparamagnetism for efficient magnetic separation (Fig. 5).

Raman spectroscopy was employed to further confirm the structural features of GO and the final nanocomposite GO/Fe_3O_4@SiO_2@CA. The GO spectrum showed two major peaks: At ~ 1357 cm^{-1}, the D band appears, attributed to the A_1g breathing vibration of disordered sp^3 carbons, whereas the G band at ~ 1594 cm^{-1} corresponds to the E_2g mode of sp^2 carbon domains. The intensity ratio (I_D/I_G) was calculated to be ~ 1.02, indicating a moderate degree of disorder and oxidation in the GO structure. After the functionalization and coating steps, the Raman spectrum of GO/Fe_3O_4@SiO_2@CA maintained both D and G bands with minor shifts and broadening, suggesting successful integration without significant degradation of the GO framework. A broad peak at ~ 2650 cm^{-1} (2D band) was also observed, which is characteristic of few-layered graphene oxide (Fig. 6).

The thermal behavior of the (a) GO@Fe_3O_4, (b) GO@Fe_3O_4@SiO_2 and (c) GO@Fe_3O_4@SiO_2@CA nanoparticles was estimated by TGA analysis (Fig. 7). Results depict appropriate thermal stability with no significant decline in weight. TGA curves revealed initial weight loss below 200 °C due to moisture and solvent removal. Further loss (~ 23%) between 200 and 600 °C is attributed to the decomposition of grafted citric acid and labile groups (Fig. 7c).

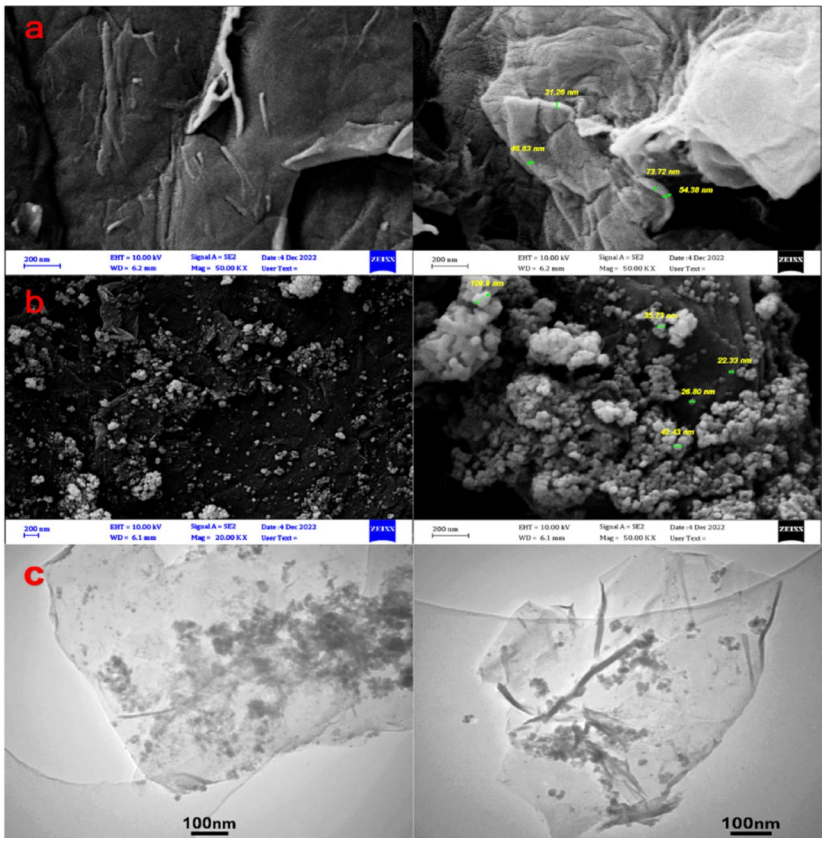


Fig. 3. FE-SEM of (**a**) GO, (**b**) GO@Fe_3O_4@SiO_2@CA and (**c**) TEM of GO@Fe_3O_4@SiO_2@CA.

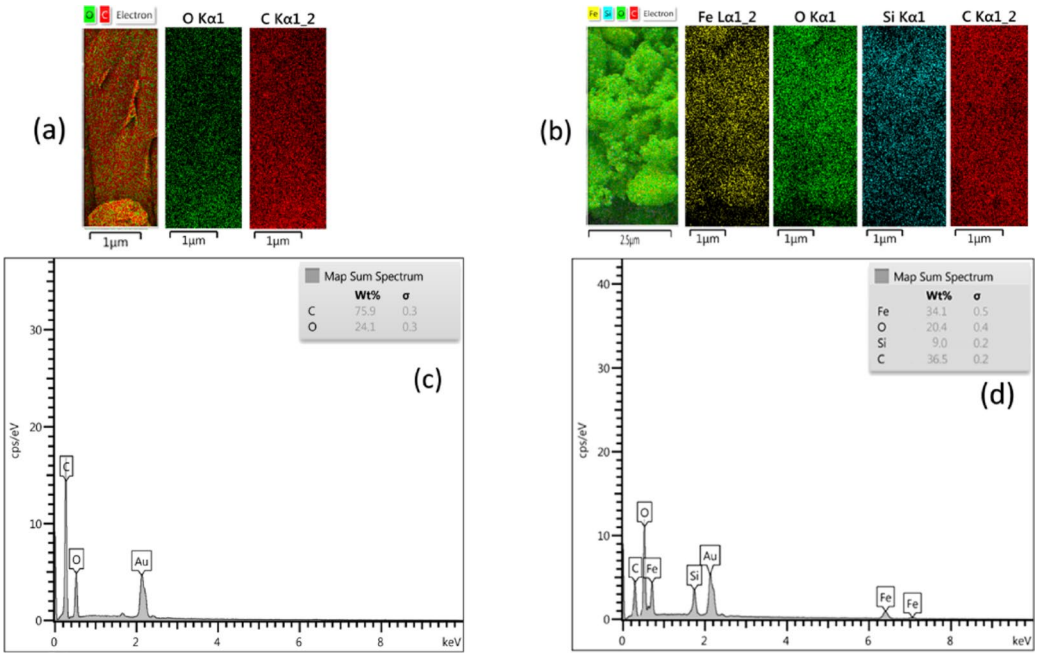


Fig. 4. Elemental mapping images of (**a**) GO, (**b**) GO@Fe_3O_4@SiO_2@CA and EDX analysis of (**c**) GO, (**d**) GO@Fe_3O_4@SiO_2@CA nanocomposite.

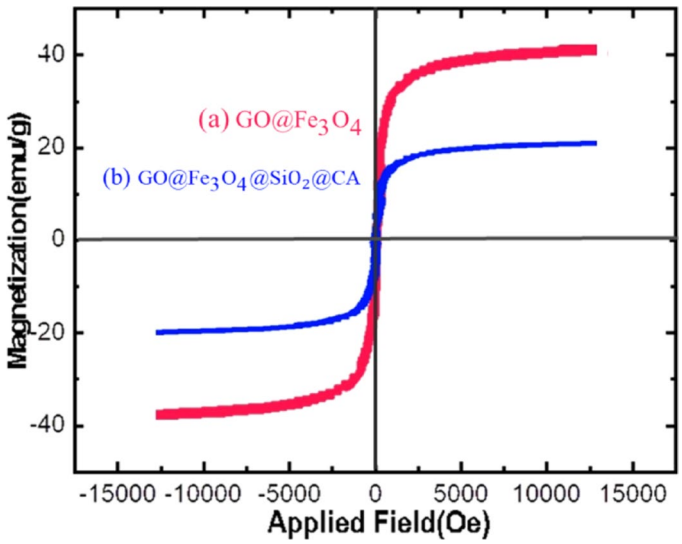


Fig. 5. VSM magnetization curves of (a) GO@Fe_3O_4 and (b) GO@Fe_3O_4@SiO_2@CA nanocomposite.

Catalytic performance in naphthopyranopyrimidine synthesis

The catalytic performance of GO/Fe_3O_4@SiO_2@CA was evaluated in the three-component reaction of β-naphthol, barbituric acid, and various aromatic aldehydes in ethanol under ultrasonic irradiation. The reaction conditions were mild (60 °C, 80 W), and the products were obtained in excellent yields (88–97%) within 10–20 min. The nanocatalyst enabled rapid C–C and C–N bond formation through a one-pot condensation pathway. Electron-donating and electron-withdrawing groups on the aldehydes did not significantly affect the yields, indicating the broad applicability of the catalyst. The calculation of Turnover Number (TON) and Turnover Frequency (TOF) are also given below.

Optimization of reaction conditions

To identify the optimal conditions for the synthesis of naphthopyranopyrimidine derivatives, the effects of three main variables: catalyst amount, ultrasonic power, and solvent type—were investigated using a model reaction between β-naphthol, barbituric acid, and 4-chlorobenzaldehyde at 60 °C. (Fig. 8)

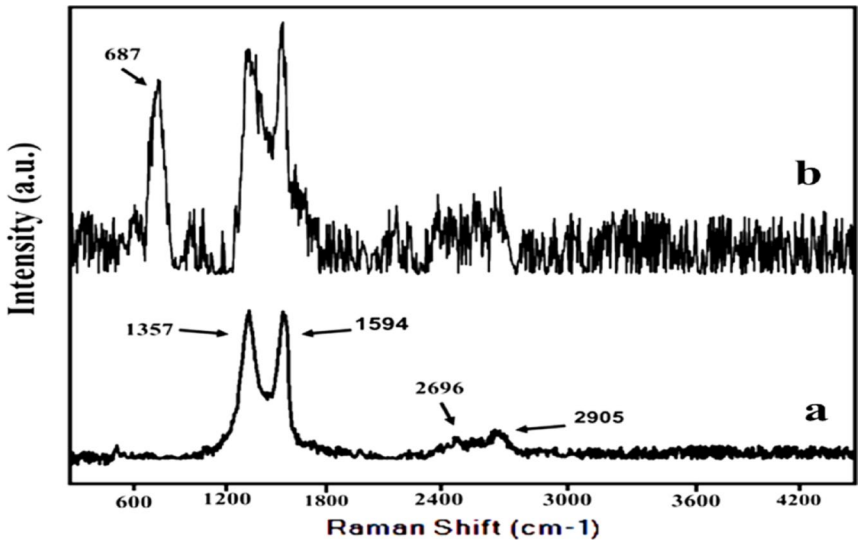


Fig. 6. Raman spectra of (a) GO and (b) GO@Fe_3O_4@SiO_2@CA nanocomposite.

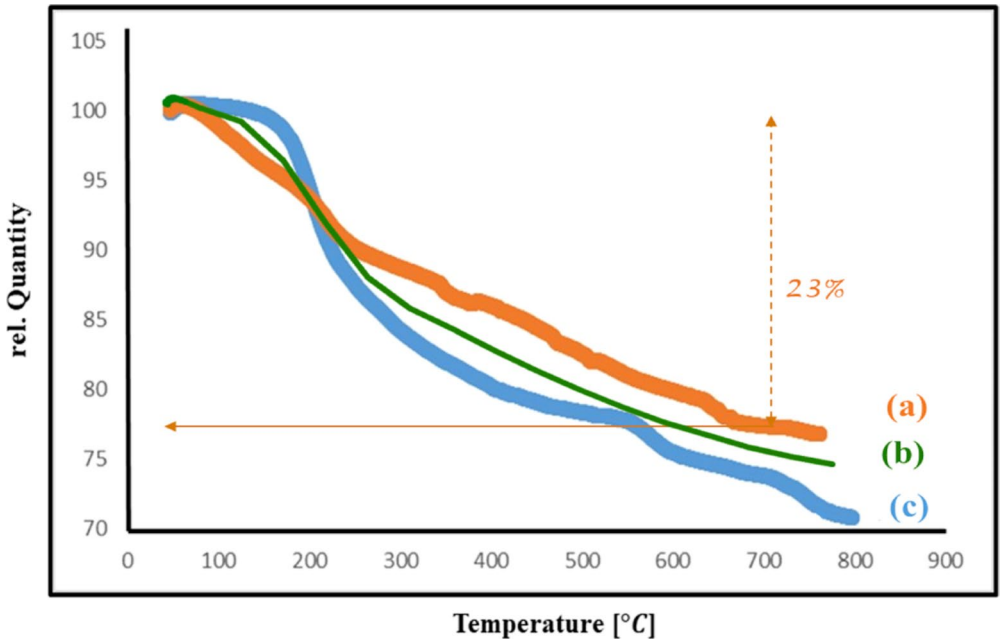


Fig. 7. TGA thermograms of (a) GO@Fe_3O_4, (b) GO@Fe_3O_4@SiO_2 and (c) GO@Fe_3O_4@SiO_2@CA nanocatalyst.

Catalyst amount

Different amounts of the GO@Fe_3O_4@SiO_2@CA nanocatalyst (15, 20, 25, and 30 mg) were tested under constant ultrasonic power (80 W) in ethanol. As shown in Table 1, the reaction proceeded efficiently at all catalyst loadings, but the yield increased with higher catalyst amounts. Maximum yield (97%) was obtained with 25 and 30 mg within 10 min. Therefore, 25 mg was selected as the optimal loading.

Ultrasonic power

To evaluate the influence of ultrasound intensity, reactions were performed using different power levels (40, 60, 80, and 100 W) while keeping the other parameters constant. The results are presented in Table 2. It was found that 80 W provided the best outcome with a 97% yield in 10 min. Increasing the power beyond this level did not significantly enhance the yield.

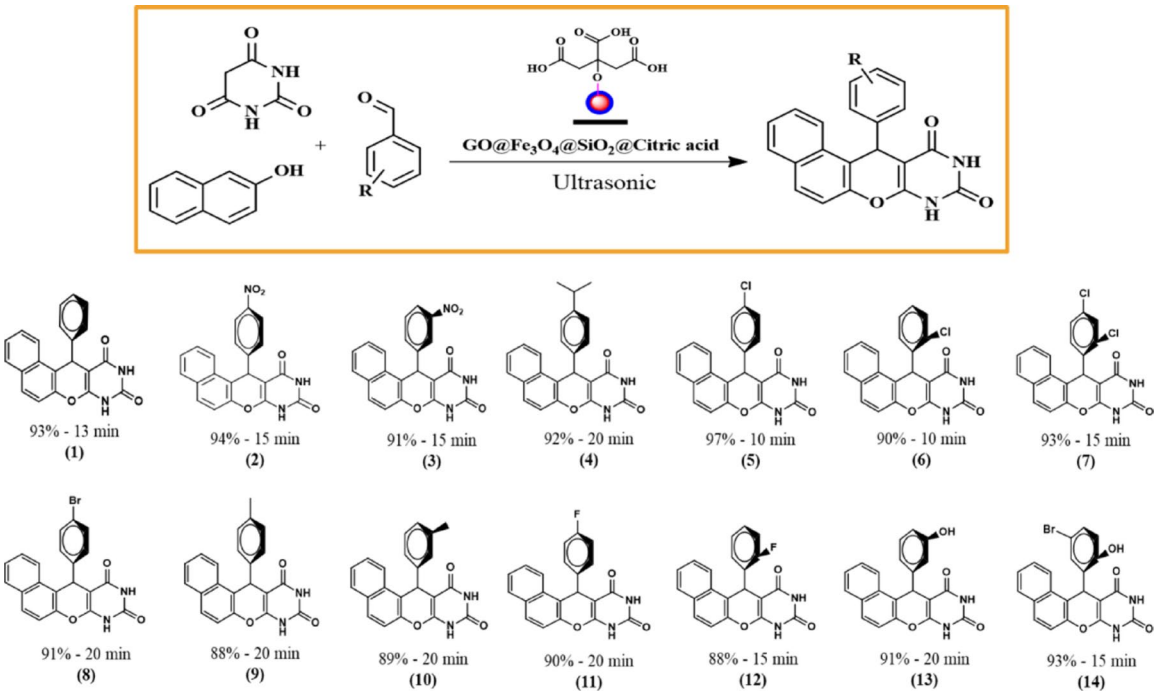


Fig. 8. Optimization of the reaction conditions for the synthesis of naphthopyranopyrimidines using GO/Fe_3O_4@SiO_2@CA under ultrasonic irradiation.

Entry	Catalyst (mg)	Time (min)	Yield (%)[b]
1	15	10	89
2	20	10	93
3	25	10	97
4	30	10	97

Table 1. Reported catalytic system for the formation of spiro[indene-2,2'-naphthalene]−4'-carbonitriles[a]. [a]Reaction conditions: 4-chlorobenzaldehyde (1 mmol), barbituric acid (1 mmol), and 2-naphthol (1.5 mmol) in the presence of GO@Fe_3O_4@SiO_2@CA as catalyst in EtOH under Ultrasonic irradiation (80 W). [b]Isolated yields.

Entry	Ultrasonic Power (W)	Time (min)	Yield[b] (%)
1	40	10	75
2	60	10	87
3	80	10	97
4	100	10	97

Table 2. Effect of ultrasonic power on the model reaction[a]. [a]Reaction conditions: 4-chlorobenzaldehyde (1 mmol), barbituric acid (1 mmol), and 2-naphthol (1.5 mmol) in the presence of GO@Fe_3O_4@SiO_2@CA (25 mg) as catalyst in EtOH. [b]Isolated yields.

Solvent screening

Various solvents were examined to determine their effect on the efficiency of the reaction. As shown in Table 3, dry ethanol afforded the highest yield (97%) in just 10 min. Other solvents such as water-ethanol mixtures, acetonitrile, DMF, and DMSO resulted in significantly lower yields. Thus, ethanol was selected as the optimal and green solvent for subsequent reactions.

Turnover number (TON) and turnover frequency (TOF)

To evaluate the intrinsic catalytic efficiency of the prepared nanocomposite, the turnover number (TON) and turnover frequency (TOF) were calculated based on the amount of active acidic sites estimated from thermogravimetric analysis (TGA). TGA analysis indicated that approximately 23 wt% of the catalyst corresponds

Entry	Entry Solvent	Time (min)	Yield[b] (%)
1	Ethanol (dry)	10	97
2	Ethanol/water (1:1)	10	45
3	Acetonitrile	10	65
4	DMF	10	56
5	DMSO	10	55

Table 3. Effect of solvent on reaction yield[a]. [a]Reaction conditions: 4-chlorobenzaldehyde (1 mmol), barbituric acid (1 mmol), and 2-naphthol (1.5 mmol) in the presence of GO@Fe_3O_4@SiO_2@CA as catalyst under Ultrasonic irradiation (80 W). [b]Isolated yields.

Entry	Aldehyde	Yield[b] (%)	Time (min)	Melting point[c]
1	Benzaldehyde	93	13	353–355[31]
2	4-Nitrobenzaldehyde	94	15	373–376[31]
3	3-Nitrobenzaldehyde	91	15	374–376[31]
4	4-Isopropylbenzaldehyde	92	20	472–476
5	4-Chlorobenzaldehyde	97	10	358–361[31]
6	2-Chlorobenzaldehyde	90	10	376–379[49]
7	2,4-Dichlorobenzaldehyde	93	15	425–429
8	4-Bromobenzaldehyde	91	20	292–295[31]
9	4-Methylbenzaldehyde	88	20	358–360[31]
10	3-Methylbenzaldehyde	89	20	363–369
11	4-Fluorobenzaldehyde	90	20	354–357[50]
12	2-Fluorobenzaldehyde	88	15	354–358
13	3-Hydroxybenzaldehyde	91	20	450–453
14	5-Bromo-2-hydroxybenzaldehyde	93	15	480–486

Table 4. Naphthopyranopyrimidine derivatives synthesized under ultrasonic conditions[a]. [a]Reaction conditions: benzaldehyde derivatives (1 mmol), barbituric acid (1 mmol), and 2-naphthol (1.5 mmol) in the presence of GO@Fe_3O_4@SiO_2@CA (25 mg) as catalyst in EtOH under Ultrasonic irradiation (80 W). [b]Isolated yields. [c]Reference.

to immobilized citric acid. The calculation of active sites was performed assuming that each citric acid molecule provides three Brønsted acidic (–COOH) groups. Based on the molar mass of citric acid (192.12 g mol^{-1}), the number of moles of citric acid incorporated into the catalyst was estimated from the TGA weight loss, and the total acidic sites were determined accordingly. In a typical reaction, 25 mg of catalyst was used for the conversion of 1 mmol of barbituric acid (limiting reagent in the model reaction between β-naphthol, barbituric acid, and 4-chlorobenzaldehyde), affording 97% yield within 10 min under ultrasonic irradiation. The turnover number (TON) was calculated using the following Eq. (1):

$$TON = \frac{moles\ of\ product\ formed}{moles\ of\ active\ scidic\ sites} \tag{1}$$

The TON value was found to be approximately 11, indicating that each acidic site participates in multiple catalytic cycles. The turnover frequency (TOF) was calculated according to Eq. (2):

$$TOF = \frac{TON}{reaction\ time} \tag{2}$$

A TOF value of approximately 65 h^{-1} was obtained. These results confirm that the catalytic activity originates from accessible surface acidic sites introduced by immobilized citric acid, rather than from stoichiometric consumption of functional groups[48].

One-pot synthesis of naphthopyranopyrimidine derivatives under ultrasound irradiation

The catalytic performance of GO@Fe_3O_4@SiO_2@CA was evaluated in the synthesis of 12,8-dihydro-9H-naphtho[2',1':4,5]pyrano[2,3-d]pyrimidine-11,9(H)-dione derivatives. A series of aromatic aldehydes with varying electronic substituents were reacted with β-naphthol and barbituric acid under ultrasound-assisted conditions (80 W, 40 kHz) using 25 mg of the nanocatalyst. The reaction times and isolated yields are summarized in Table 4.

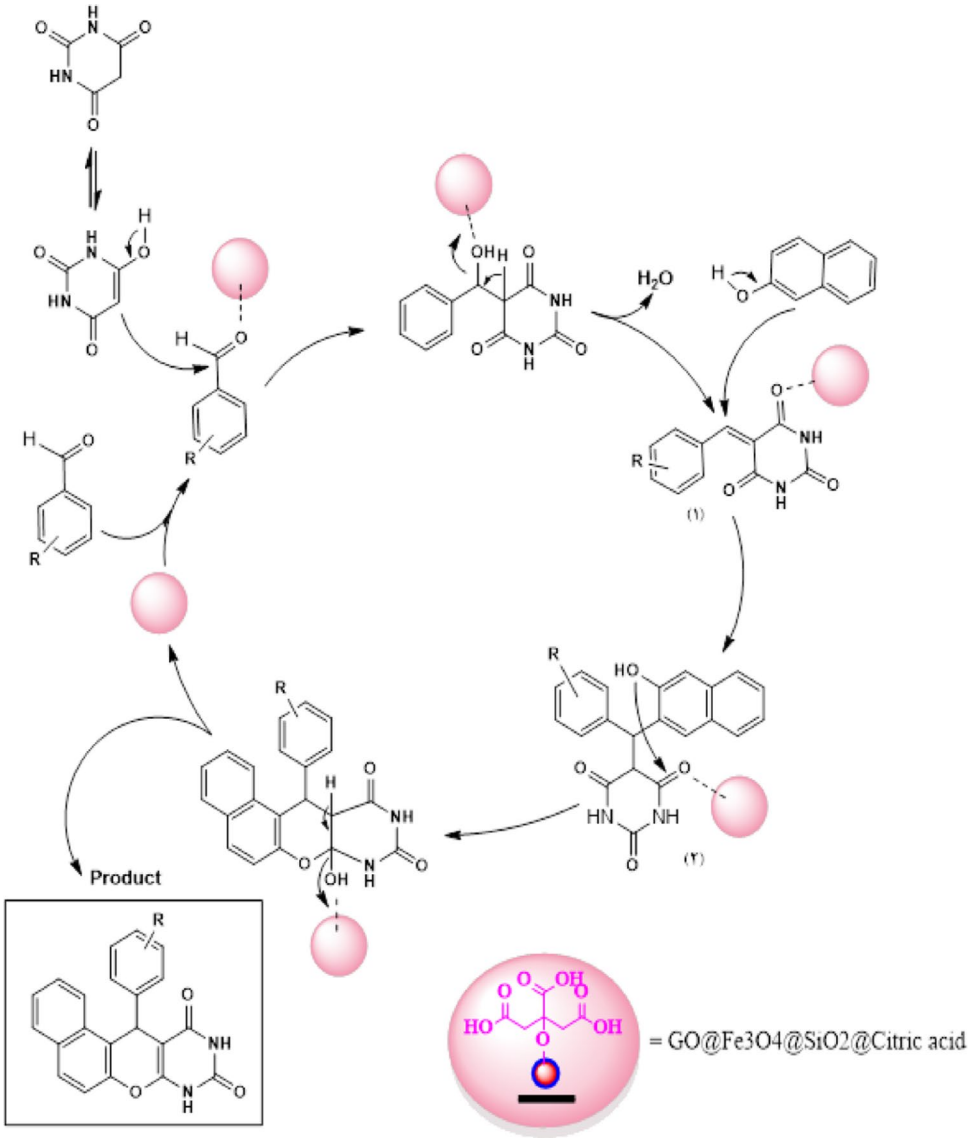
The results indicate that both electron-donating and electron-withdrawing groups on the aromatic ring had minimal effect on product yields. All products were obtained in excellent yields (88–97%) within short reaction

times (10–20 min), demonstrating the efficiency of the nanocatalyst under mild and green conditions. Upon completion of the time reaction which was monitored by TLC (n-hexane/ethyl acetate: 6:4) the crude precipitate was filtered off and purified by recrystallization from ethanol to obtain pure product.

These results highlight the potential of GO@Fe_3O_4@SiO_2@CA as an efficient and reusable nanocatalyst for green multicomponent synthesis of biologically active heterocycles.

Proposed reaction mechanism

The plausible mechanism for the synthesis of naphthopyranopyrimidines using β-naphthol, barbituric acid, and aromatic aldehydes in the presence of the acidic nanocatalyst GO/Fe_3O_4@SiO_2@CA is illustrated in Scheme 3. In the first step, the carbonyl group of the aldehyde is activated through protonation by the acidic sites of the nanocatalyst. The activated aldehyde undergoes a Knoevenagel-type condensation with barbituric acid to form intermediate (I). Subsequently, β-naphthol attacks the activated carbon of intermediate (I) via a Michael addition, generating intermediate (II). This intermediate then undergoes intramolecular cyclization, in which the hydroxyl group of β-naphthol attacks the carbonyl group of the barbituric acid moiety, affording a six-membered heterocyclic ring. Finally, dehydration of the intermediate produces the desired naphthopyranopyrimidine derivative under ultrasonic conditions (Scheme 3). A second mechanism has also been predicted in other articles. The first step involves the formation of intermediate which was formed by the nucleophilic attack of 2-naphthol to aldehyde and elimination of one H_2O molecule. Adsorption of the aldehyde on the catalyst surface enhances the electrophilicity of the carbonyl group which is followed by the nucleophilic attack of 2-naphthol



Scheme 3. Plausible mechanism for the synthesis of naphthopyranopyrimidines catalyzed by GO/Fe_3O_4@SiO_2@CA under ultrasonic conditions.

to them. Then, Michael addition of intermediate is formed with cyclic 1,3-dicarbonyl compound followed by cyclodehydration yield the desired final product[50].

All products were characterized by melting point (m.p.), FT-IR, ^{1}H NMR, ^{13}C NMR and elemental microanalysis. The Spectra data of new compounds are presented:

12-(2,4-Dichlorophenyl)−8,12-dihydro-9H-naphtho[2',1':5,6]pyrano[2,3-d]pyrimidine-9,11(H10)-dione (7). White solid, yield 92%, M.P (°C): 425–429. IR (KBr)/ῡ (cm^{-1}): 3444 (N–H stretch), 2927 (C–H stretch), 1711 (C = O amide), 1653 (N–H bending), 1515–1452 (C = C alkene), 1359 (C–N stretch), 1270 (C–O). ^{1}H NMR (DMSO-d_6, 400 MHz)/δ (ppm): 5.85 (s, 1 H), 7.27 (dd, 1 H, J = 8 Hz, J = 2.4 Hz, Ar–H), 7.39–7.55 (m, 5 H, Ar–H), 7.94–8.01 (m, 3 H, Ar–H), 11.05 (s, NH), 12.13 (s, NH). ^{13}C NMR (DMSO-d_6, 100 MHz)/δ (ppm): 163.51, 154.81, 154.01, 150.16, 149.18, 133.53, 131.45, 130.78, 129.12, 128.64, 128.32, 127.57, 127.10, 123.61, 122.87, 122.85, 119.23, 118.09, 116.39, 87.36, 29.05. Anal. Calcd. for $C_{21}H_{12}Cl_2N_2O$. (See SI, Figs. S7-S9)

12-(3-Methylphenyl)−8,12-dihydro-9H-naphtho[2',1':5,6]pyrano[2,3-d]pyrimidine-9,11(H10)-dione (10). White solid, yield 89%, M.P (°C): 363–369. IR (KBr)/ῡ (cm^{-1}): 3253 (N–H stretch), 3132 (overtone), 1709 (C = O amide), 1657 (N–H bending), 1509–1401 (C = C alkene), 1346 (C–N stretch), 1258 (C–O). ^{1}H NMR (DMSO-d_6, 400 MHz)/δ (ppm): 5.54 (s, 1 H), 6.90 (d, 1 H, J = 8 Hz, Ar–H), 7.03–7.13 (m, 3 H, Ar–H), 7.47–7.53 (m, 3 H, Ar–H), 7.94–7.99 (m, 2 H, Ar–H), 8.02 (d, 1 H, J = 8 Hz, Ar–H), 11.05 (s, NH), 12.08 (s, NH). ^{13}C NMR (DMSO-d_6, 100 MHz)/δ (ppm): 163.50, 153.84, 150.05, 147.14, 145.02, 137.73, 131.69, 130.89, 130.04, 129.04, 128.95, 128.53, 127.80, 127.64, 125.82, 125.74, 124.10, 117.60, 117.16, 90.33, 35.05, 21.51. Anal. Calcd. for $C_{22}H_{16}N_2O$. (See SI, Figs. S19-S21)

12-(2-Fluorophenyl)−8,12-dihydro-9H-naphtho[2',1':5,6]pyrano[2,3-d]pyrimidine-9,11(10 H)-dione (12). White solid, yield 89%, M.P (°C): 354–358. IR (KBr)/ῡ (cm^{-1}): 3424 (N–H stretch), 3235 (overtone), 1709 (C = O amide), 1654 (N–H bending), 1508 (C = C alkene), 1400 (C–N stretch), 1248 (C–O). ^{1}H NMR (DMSO-d_6, 400 MHz)/δ (ppm): 5.74 (s, 1 H), 7.03–7.07 (m, 2 H, Ar–H), 7.13–7.19 (m, 1 H, Ar–H), 7.39–7.47 (m, 3 H, Ar–H), 7.54 (dd, 1 H, J = 8 Hz, J = 4 Hz, Ar–H), 7.95 (t, 2 H, J = 8 Hz, Ar–H), 8.02 (d, 1 H, J = 8 Hz, Ar–H), 11.07 (s, NH), 12.12 (s, NH). ^{13}C NMR (DMSO-d_6, 100 MHz)/δ (ppm): 163.39, 158.92, 154.27, 150.07, 147.13, 131.67, 131.56, 130.92, 130.26, 129.22, 129.13, 127.95, 125.77, 124.84, 123.24, 117.17, 116.25, 116.04, 115.82, 88.65, 29.94. Anal. Calcd. for $C_{24}H_{20}N_2O_3$. (See SI, Figs. S26-S28)

12-(3-Hydroxyphenyl)−8,12-dihydro-9H-naphto[1",2":5,6]pyrano[2,3-d]pyrimidine-9,11-(H10)-dione (13). White solid, yield 91%, M.P(°C): 450–453. IR (KBr)/ῡ(cm^{-1}): 3425 (OH), 3359 (N-H stretch), 3096 (overtone), 2938 (C-H stretch), 1707 (C = O amide), 1663 (N-H bending), 1519 – 1451 (C = C alkene), 1358 (C-N stretch), 1232 (C-O). ^{1}H NMR (DMSO-d_6, 400 MHz)/δ (ppm): 5.50(s, 1H), 6.475(dd, 1H, *J* = 8 Hz, *J* = 4 Hz, Ar-H), 6.65(dd, 1H, *J* = 4 Hz, *J* = 4 Hz, Ar-H), 6.765(dd, 1H, *J* = 8 Hz, *J* = 4 Hz, Ar-H), 6.99(t, 1H, *J* = 8 Hz, Ar-H), 7.44(d, 1H, *J* = 8 Hz, Ar-H), 7.47–7.55(m, 2 H, Ar-H),7.96–8.02(m, 3 H, Ar-H) 9.25(s, OH), 11.07(s, NH), 12.08(s, NH). ^{13}C NMR (DMSO-d_6, 100 MHz) (ppm): 163.51, 157.64, 153.86, 150.02, 147.16, 146.39, 131.69, 130.93, 130.02, 129.55, 129.06, 127.81, 125.78, 124.07, 119.35, 117.68, 117.13, 115.36, 113.99, 90.31, 34.92. Anal. Calcd. For C21H14N2O4. (See SI, Figs. S29-S32)

12-(2-Hydroxy-5-bromophenyl)−8,12-dihydro-9H-naphtho[2',1':5,6]pyrano[2,3-d]pyrimidine-9,11(10 H)-dione (14). White solid, yield 93%, M.P (°C): 480–486. IR (KBr)/ῡ (cm^{-1}): 3347 (N–H stretch), 3102 (overtone), 2933 (C–H stretch), 1718 (C = O amide), 1647 (N–H bending), 1532–1427 (C = C alkene), 1359 (C–N stretch), 1291 (C–O). ^{1}H NMR (DMSO-d_6, 400 MHz)/δ (ppm): 5.92 (s, 1 H), 6.65 (d, 1 H, J = 8 Hz, Ar–H), 7.07 (d, 1 H, J = 8 Hz, Ar–H), 7.17 (dd, 1 H, J = 4 Hz, Ar–H), 7.34–7.39 (m, 2 H, Ar–H), 7.57 (dd, 1 H, J = 8 Hz, Ar–H), 7.67 (d, 1 H, J = 8 Hz, Ar–H), 7.79 (d, 1 H, J = 8 Hz, Ar–H), 8.62 (d, 1 H, J = 8 Hz, Ar–H), 9.58 (s, OH), 10.82 (s, NH), 11.86 (s, NH). ^{13}C NMR (DMSO-d_6, 100 MHz)/δ (ppm): 163.51, 154.81, 154.01, 150.16, 149.18, 133.53, 131.45, 130.78, 129.12, 128.64, 128.32, 127.57, 127.10, 123.61, 122.87, 122.85, 119.23, 118.09, 116.39, 87.36, 29.05. Anal. Calcd. for C21H13BrN2O4. (See SI, Figs. S33-S35)

Catalyst recyclability

An essential feature of heterogeneous nanocatalysts is their structural stability and reusability over multiple cycles without significant loss in activity. To evaluate the reusability of the GO@Fe_3O_4@SiO_2@CA nanocatalyst, recycling experiments were conducted using the model reaction between β-naphthol, barbituric acid, and 4-chlorobenzaldehyde under the optimized ultrasonic conditions. After each cycle, the catalyst was magnetically separated, thoroughly washed with ethanol and water, and dried under vacuum before reuse. The yield of the reaction was measured after each run to assess catalytic efficiency. As shown in Fig. 9, the catalyst maintained high activity over seven consecutive cycles. As it can be viewed, the catalytic activity of nanocomposite declined from 97% in the fresh run to 89% after the completion of seven run.

*This behavior indicating excellent operational stability under ultrasonic conditions. The heterogeneous process is also checked for the model reaction. For this purpose, the catalyst was separated from the reaction mixture after 5 min and the reaction yield was estimated to be around 74%. Then, the reaction continued without catalyst for another 10 min. The obtained product had no significant increase in yield (~78%). According to the mentioned results, presence of the catalyst until the end of the reaction is necessary to reach the best yield. Furthermore, FT-IR, XRD, SEM and TEM analyses of the recovered catalyst after the seven cycle revealed no major changes in structure, confirming that the catalyst remained stable (Fig. 10).

Comparison with other catalysts

To evaluate the efficiency and advantages of GO@Fe_3O_4@SiO_2@CA as a nanocatalyst, its performance was compared with several previously reported catalysts used for the synthesis of similar heterocyclic compounds (Table 5). According to the date, conduction the model reaction without any catalyst gave only 37% after 40 min (Table 5, entry 1). We also investigated the catalytic activity of GO@Fe_3O_4@SiO_2 and CA. Based on our empirical experiment, CA which was modified on the surface of Fe_3O_4@SiO_2@SiO_2 indicated the best catalytic

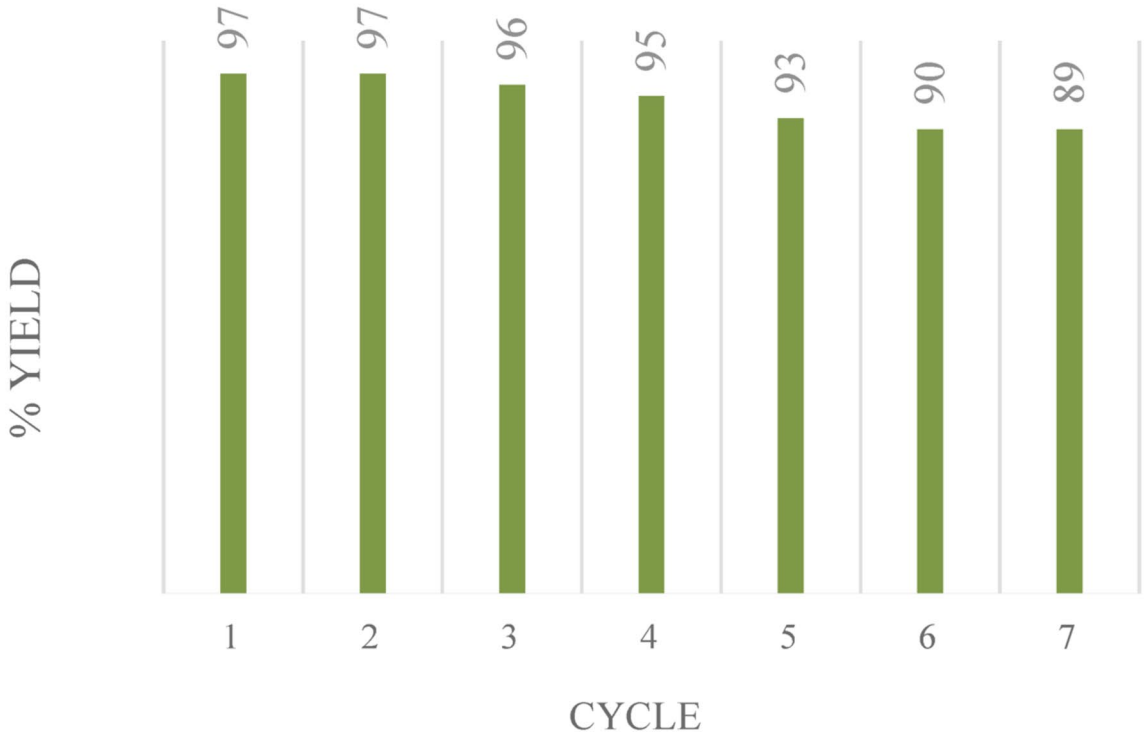


Fig. 9. Reusability of the GO/Fe_3O_4@SiO_2@CA nanocatalyst.

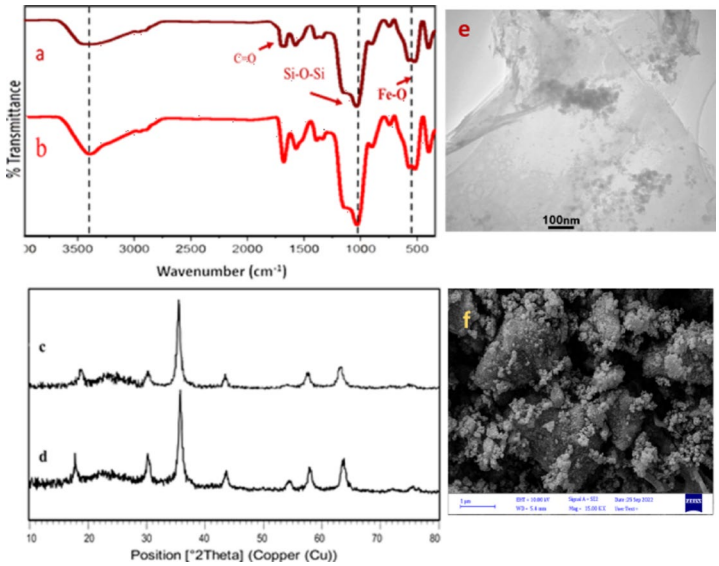


Fig. 10. FT-IR spectrum of GO/Fe_3O_4@SiO_2@CA (a) after and (b) before seven reaction cycles, XRD pattern of GO/Fe_3O_4@SiO_2@CA (c) after and (d) before seven reaction cycles, (e) TEM and (f) FE-SEM of GO/Fe_3O_4@SiO_2@CA after seven reaction cycles.

performance in the reaction. Moreover, it was discovered that in the presence of GO@Fe_3O_4@SiO_2@CA at 25 mg, the reaction rate and yield were considerably increased (Table 5, entry 2). Compared to homogeneous or metal-based catalysts such as Fe_3O_4@MCM-48-SO_3H, MWCNTs@NHBut/PTA and $ZnAl_2O_4$, the current nanocomposite demonstrated several significant advantages, including:

- Higher product yields (up to 97%).

Entry	Catalyst	Time (min)	Temp. (◦C) or Power (W)	Yield (%)[b]	Ref.
1	-	30	80 W	37	This work
2	GO@Fe_3O_4@SiO_2@CA (25 mg)	10	80 W	97	This work
3	GO@Fe_3O_4@SiO_2 (25 mg)	30	80 W	63	This work
4	CA (25 mg)	30	80 W	76	This work
5	Fe_3O_4@MCM-48-SO_3H (50 mg)	45	25 °C	89	[32]
6	MWCNTs@NHBut/PTA) (25 mg)	25	100 °C	86	[51]
7	$ZnAl_2O_4$ (0.7 mol%)	10	500 W (MW)	88	[52]

Table 5. Reported catalytic system for the formation of spiro[indene-2,2'-naphthalene]–4'-carbonitriles[a]. [a]Reaction conditions: 4-chlorobenzaldehyde (1 mmol), barbituric acid (1 mmol), and 2-naphthol (1.5 mmol) in the presence of GO@Fe_3O_4@SiO_2@CA as catalyst in EtOH under Ultrasonic irradiation (80 W). [b]Isolated yields.

- Shorter reaction times (10–20 min).
- Mild ultrasonic-assisted conditions (60 °C, EtOH).
- Easy magnetic recovery and excellent recyclability (up to 7 cycles with minimal loss).
- Eco-friendly nature with non-toxic, inexpensive materials.

Moreover, the use of ultrasound irradiation significantly improved mass transfer and surface activation of the nanocatalyst, further enhancing catalytic efficiency. In contrast, other systems often required longer reaction times, higher temperatures, use of toxic solvents, or complex catalyst synthesis procedures. Therefore, the developed GO/Fe_3O_4@SiO_2@CA system provides a green, efficient, and reusable alternative for the sustainable synthesis of biologically relevant heterocycles.

Conclusion

In summary, we successfully developed a green, efficient, and magnetically recoverable nanocatalyst based on GO@Fe_3O_4@SiO_2 functionalized with citric acid. The nanocatalyst was thoroughly characterized using FT-IR, XRD, FE-SEM, TEM, EDX, TGA, VSM, and Raman spectroscopy, confirming its core–shell structure, functional groups, thermal stability, and magnetic behavior. The catalyst showed excellent performance in the one-pot ultrasound-assisted synthesis of naphthopyranopyrimidine derivatives under mild and environmentally friendly conditions. A wide range of products was obtained in high yields (88–97%) within short times (10–20 min), and the catalyst was efficiently recycled for at least five consecutive runs with minimal loss in activity. Compared to other catalytic systems, the GO@Fe_3O_4@SiO_2@CA nanocatalyst offered a superior combination of high efficiency, operational simplicity, recyclability, and green chemistry principles. These findings suggest that this system is a promising candidate for sustainable synthesis of biologically active heterocyclic compounds.

Data availability

All spectral data including FTIR, 1 H NMR, and 13 C NMR spectra for the synthesized naphthopyranopyrimidines and also reaction conditions for the synthesis of naphthopyranopyrimidines using GO/Fe_3O_4@SiO_2@CA under ultrasonic irradiation are provided in the Supporting Information.

Received: 13 November 2025; Accepted: 4 May 2026
Published online: 18 May 2026

References

1. Tomar, S. Innovative nanotechnology applications in automobiles. *Int. J. Eng. Res. Technol.* **1**, 2493 (2012).
2. Saleh, T. A. Nanomaterials: Classification, properties, and environmental toxicities. *Environ. Technol. Innov.* **20**, 101067 (2020).
3. Potbhare, A. K. et al. Bioinspired graphene-based metal oxide nanocomposites for photocatalytic and electrochemical performances: An updated review. *Nanoscale Adv.* **6**, 2539–2568 (2024).
4. Li, X. & Wang, J. One-dimensional and two-dimensional synergized nanostructures for high-performing energy storage and conversion. *InfoMat* **2**, 3–32 (2020).
5. Yang, G., Li, L., Lee, W. B. & Ng, M. C. Structure of graphene and its disorders: A review. *Sci. Technol. Adv. Mater.* **19**, 613–648 (2018).
6. Choi, W., Lahiri, I., Seelaboyina, R. & Kang, Y. S. Synthesis of graphene and its applications: A review. *Crit. Rev. Solid State Mater. Sci.* **35**, 52–71 (2010).
7. Pyrzynska, K. Use of nanomaterials in sample preparation. *TRAC Trends Anal. Chem.* **43**, 100–108 (2013).
8. Lee, H. S. et al. Electromagnetic shielding performance of carbon black mixed concrete with Zn–Al metal thermal spray coating. *Materials* **13**, 895 (2020).
9. Qiu, T., Yang, J.-G. & Bai, X.-J. Preparation of coal-based graphite with different microstructures by adjusting the content of ash and volatile matter in raw coal. *Energy Sources. A. Util. Environ. Eff.* **42**, 1874–1881 (2020).
10. Wu, S. et al. Fe3O4 magnetic nanoparticles synthesis from tailings by ultrasonic chemical co-precipitation. *Mater. Lett.* **65**, 1882–1884 (2011).
11. Ding, H. et al. Fe3O4@ SiO2 core/shell nanoparticles: The silica coating regulations with a single core for different core sizes and shell thicknesses. *Chem. Mater.* **24**, 4572–4580 (2012).

12. Zubir, N. A., Yacou, C., Motuzas, J., Zhang, X. & Diniz da Costa, J. C. Structural and functional investigation of graphene oxide–Fe3O4 nanocomposites for the heterogeneous Fenton-like reaction. *Sci. Rep.* **4**, 4594 (2014).
13. Ebrahimi-Tazangi, F., Hekmatara, S. H. & Seyed-Yazdi, J. Remarkable microwave absorption of GO-SiO2/Fe3O4 via an effective design and optimized composition. *J. Alloys Compd.* **854**, 157213 (2021).
14. Yang, X. et al. Superparamagnetic graphene oxide–Fe_3O_4 nanoparticles hybrid for controlled targeted drug carriers. *J. Mater. Chem.* **19**, 2710–2714 (2009).
15. Maleki, A., Hajizadeh, Z. & Abbasi, H. Surface modification of graphene oxide by citric acid and its application as a heterogeneous nanocatalyst in organic condensation reaction. *Carbon Lett.* **27**, 42–49 (2018).
16. Raza, Z. A., Shabbir, M., Majeed, M. I. & Tawab, A. Development of citric acid grafted graphene oxide nanosheets as nanocatalyst in the synthesis of an imidazole derivative. *Inorg. Nano-Metal Chem.* **55**, 352–361 (2025).
17. Namvari, M. & Namazi, H. Synthesis of magnetic citric-acid-functionalized graphene oxide and its application in the removal of methylene blue from contaminated water. *Polym. Int.* **63**, 1881–1888 (2014).
18. Dehghani-Dashtabi, M., Hekmatara, H. & Seyed-Yazdi, J. Highly magnetic nanocomposites consist of magnetite nanoparticles, graphene oxide and hyper-branched poly citric acid. *Mater. Chem. Phys.* **224**, 271–278 (2019).
19. Oboudatian, H. S., Naeimi, H. & Moradian, M. A Brønsted acidic ionic liquid anchored to magnetite nanoparticles as a novel recoverable heterogeneous catalyst for the Biginelli reaction. *RSC Adv.* **11**, 7271–7279 (2021).
20. Ge, H., Wang, C., Liu, S. & Huang, Z. Synthesis of citric acid functionalized magnetic graphene oxide coated corn straw for methylene blue adsorption. *Bioresour. Technol.* **221**, 419–429 (2016).
21. Mu, Y. F. et al. Ultrathin and small-size graphene oxide as an electron mediator for perovskite-based Z-scheme system to significantly enhance photocatalytic CO2 reduction. *Small* **16**, 2002140 (2020).
22. Chen, J. et al. New methylene blue covalently functionalized graphene oxide nanocomposite as interfacial material for the electroanalysis of hydrogen peroxide. *Front. Chem.* **9**, 788804 (2021).
23. Sharif Nasirian, V., Shahidi, S. A., Tahermansouri, H. & Chekin, F. Application of graphene oxide in the adsorption and extraction of bioactive compounds from lemon peel. *Food Sci. Nutr.* **9**, 3852–3862 (2021).
24. Majumder, P. & Gangopadhyay, R. Evolution of graphene oxide (GO)-based nanohybrid materials with diverse compositions: An overview. *RSC Adv.* **12**, 5686–5719 (2022).
25. Khojastehnezhad, A. et al. Size-dependent catalytic activity of palladium nanoparticles decorated on core–shell magnetic microporous organic networks. *ACS Appl. Nano Mater.* **6**, 17706–17717 (2023).
26. Keyhaniyan, M., Khojastehnezhad, A., Eshghi, H. & Shiri, A. Magnetic covalently immobilized nickel complex: A new and efficient method for the Suzuki cross-coupling reaction. *Appl. Organomet. Chem.* **35**, e6158 (2021).
27. Khojastehnezhad, A., Maleki, B., Karrabi, B. & Seresht, E. R. Synthesis of highly functionalized piperidines using polyphosphoric acid supported on silica-coated magnetic nanoparticles. *Org. Prep. Proced. Int.* **49**, 338–345 (2017).
28. Younus, H. A. et al. Multicomponent reactions (MCR) in medicinal chemistry: A patent review (2010–2020). *Expert Opin. Ther. Pat.* **31**, 267–289 (2021).
29. Nandi, S. et al. One-pot multicomponent reaction: A highly versatile strategy for the construction of valuable nitrogen-containing heterocycles. *ChemistrySelect* **7**, e202201901 (2022).
30. Kitamura, N. & Onishi, A. Pyrimidopyrimidinedione derivatives and their use antiallergic agent. Eur Patant 163599 (1984).
31. Bedair, A. H., Emam, H. A., El-Hady, N. A., Ahmed, K. A. & El-Agrody, A. M. Synthesis and antimicrobial activities of novel naphtho [2, 1-b] pyran, pyrano [2, 3-d] pyrimidine and pyrano [3, 2-e][1, 2, 4] triazolo [2, 3-c]-pyrimidine derivatives. *Il Farmaco* **56**, 965–973 (2001).
32. Kefayati, H., Golshekan, M., Shariati, S. & Bagheri, M. Fe3O4@ MCM-48–SO3H: An efficient magnetically separable nanocatalyst for the synthesis of benzo [f] chromeno [2, 3-d] pyrimidinones. *Chin. J. Catal.* **36**, 572–578 (2015).
33. Ebrahimi, Z., Davoodnia, A., Motavalizadehkakhky, A. & Mehrzad, J. Synthesis of benzo [f] chromeno [2, 3-d] pyrimidines via the tandem intramolecular Pinner/Dimroth rearrangement and their antibacterial and antioxidant evaluation. *Org. Prep. Proced. Int.* **51**, 357–367 (2019).
34. El-Khateeb, A. Y., Hamed, S. E. & Elattar, K. M. Recent advancements in the multicomponent synthesis of heterocycles integrated with a pyrano [2, 3-d] pyrimidine core. *RSC Adv.* **12**, 11808–11842 (2022).
35. Javahershenas, R. & Nikzat, S. Recent advances in the multicomponent synthesis of heterocycles using tetronic acid. *RSC Adv.* **13**, 16619–16629 (2023).
36. Azimi, S. C. L-Proline catalyzed synthesis of naphthopyranopyrimidines via multicomponent reaction. *Iranian J. Catalysis* **5** (2015).
37. Hummers, W. S. Jr & Offeman, R. E. Preparation of graphitic oxide. *J. Am. Chem. Soc.* **80**, 1339–1339 (1958).
38. Yadav, M., Rhee, K. Y., Park, S. J. & Hui, D. Mechanical properties of Fe3O4/GO/chitosan composites. *Compos. Part. B: Eng.* **66**, 89–96 (2014).
39. Méndez-Lozano, N., Pérez-Reynoso, F. & González-Gutiérrez, C. Eco-friendly approach for graphene oxide synthesis by modified hummers method. *Materials* **15**, 7228 (2022).
40. Alam, S. N., Sharma, N. & Kumar, L. Synthesis of graphene oxide (GO) by modified Hummers method and its thermal reduction to obtain reduced graphene oxide (rGO). *Graphene* **6**, 1 (2017).
41. Alshamusi, Q. K. M., Farhan, A. M. & Khayoon, H. A. Synthesis and characterization of graphene oxide. Review 2014–2020. *Eurasian J. Phys. Chem. Math.* **7**, 125–131 (2022).
42. Marcano, D. C. et al. Improved synthesis of graphene oxide. *ACS nano*. **4**, 4806–4814 (2010).
43. Muthukumar, P., Alex, V., Pannipara, M., Al-Sehemi, A. G. & Anthony, S. P. Fabricating highly efficient Ag3PO4-Fe3O4-GO ternary nanocomposite photocatalyst: Effect of Fe3O4-GO preparation methods on photocatalytic activity. *Mater. Res. Bull.* **141**, 111337 (2021).
44. Nalbandian, L. et al. Magnetic nanoparticles in medical diagnostic applications: synthesis, characterization and proteins conjugation. *Curr. Nanosci.* **12**, 455–468 (2016).
45. Beitollahi, H., Nejad, F. G. & Shakeri, S. GO/Fe_3O_4@SiO_2 core–shell nanocomposite-modified graphite screen-printed electrode for sensitive and selective electrochemical sensing of dopamine and uric acid. *Anal. Methods* **9**, 5541–5549 (2017).
46. Hui, C. et al. Core-shell Fe 3 O 4@ SiO 2 nanoparticles synthesized with well-dispersed hydrophilic Fe 3 O 4 seeds. *Nanoscale* **3**, 701–705 (2011).
47. Shen, L., Li, B., Qiao, Y. & Song, J. Monodisperse Fe_3O_4/SiO_2 and Fe_3O_4/SiO_2/PPy core-shell composite nanospheres for IBU loading and release. *Materials* **12**, 828 (2019).
48. Hassanzadeh-Afruzi, F. *in Heterogeneous Micro and Nanoscale Composites for the Catalysis of Organic Reactions* 223–232 (Elsevier, 2022).
49. Ahmadi, M., Moradi, L. & Sadeghzadeh, M. Green synthesis of benzochromenopyrimidines in the presence of MWCNTs@ SiO2/MSA as a new and effective solid acid catalyst under microwave irradiation. *J. Mol. Struct.* **1235**, 130183 (2021).
50. Rahmatinejad, S. & Naeimi, H. Crumpled perovskite-type $LaMo_xFe_{1-x}O_3$ nanosheets: A reusable catalyst for rapid and green synthesis of naphthopyranopyrimidine derivatives. *Polyhedron* **177**, 114318 (2020).
51. Ahmadi, M., Moradi, L. & Sadeghzadeh, M. MWCNTs@ NHBut/PTA: New efficient solid acid catalyst for solvent free synthesis of benzochromenopyrimidines. *Appl. Organomet. Chem.* **33**, e4980 (2019).

52. Mohaqeq, M., Safaei-Ghomi, J., Shahbazi-Alavi, H. & Teymuri, R. $ZnAl_2O_4$ nanoparticles as efficient and reusable heterogeneous catalyst for the synthesis of 12-phenyl-8, 12-dihydro-8, 10-dimethyl-9 H-naphtho [1′, 2′: 5, 6] pyrano [2, 3-d] pyrimidine-9, 11-(10 H)-diones under microwave irradiation. *Polycycl. Aromat. Compd.* **37**, 52–62 (2017).

Acknowledgements
The authors are grateful to the University of Kashan for supporting this work.

Author contributions
R. M-M., and H. S-O. Designed and conducted some of the experiments and wrote the manuscript. J. S-G. and H. S-O. discussed the experiments, analyzed the results, and rewrite the manuscript. J. S-G. supervised the whole project. All authors reviewed the manuscript.

Declarations

Competing interests
The authors declare no competing interests.

Additional information
Supplementary Information The online version contains supplementary material available at https://doi.org/10.1038/s41598-026-52098-2.

Correspondence and requests for materials should be addressed to J.S.-G.

Reprints and permissions information is available at www.nature.com/reprints.

Publisher's note Springer Nature remains neutral with regard to jurisdictional claims in published maps and institutional affiliations.

Open Access This article is licensed under a Creative Commons Attribution-NonCommercial-NoDerivatives 4.0 International License, which permits any non-commercial use, sharing, distribution and reproduction in any medium or format, as long as you give appropriate credit to the original author(s) and the source, provide a link to the Creative Commons licence, and indicate if you modified the licensed material. You do not have permission under this licence to share adapted material derived from this article or parts of it. The images or other third party material in this article are included in the article's Creative Commons licence, unless indicated otherwise in a credit line to the material. If material is not included in the article's Creative Commons licence and your intended use is not permitted by statutory regulation or exceeds the permitted use, you will need to obtain permission directly from the copyright holder. To view a copy of this licence, visit http://creativecommons.org/licenses/by-nc-nd/4.0/.

© The Author(s) 2026